Multifractal analysis of discretized X-ray CT images for the characterization of soil macropore structures

F. San José Martínez , M.A. Martín , F.J. Caniego , M. Tuller , A. Guber , Y. Pachepsky , C. García-Gutiérrez

Technical University of Madrid (UPM), E.T.S.I. Agronomy, Department of Applied Mathematics to Agronomic Engineering, Avd. de la Complutense s/n, 28040 Madrid, Spain
The University of Arizona, Department of Soil, Water and Environmental Science, Tucson, AZ 85721, USA
Environmental Microbial Safety Laboratory, USDA-ARS-BA-ANRI-EMSL, Beltsville, MD 20705, USA

ABSTRACT

Keywords:
X-ray computed tomography of soil
Image analysis
Soil pore space
Soil spatial variability
Long-range dependence
Multifractal analysis
Hurst exponent

A correct statistical model of soil pore structure can be critical for understanding flow and transport processes in soils, and creating synthetic soil pore spaces for hypothetical and model testing, and evaluating similarity of pore spaces of different soils. Advanced visualization techniques such as X-ray computed tomography (CT) offer new opportunities of exploring heterogeneity of soil properties at horizon or aggregate scales. Simple fractal models such as fractional Brownian motion that have been proposed to capture the complex behavior of soil spatial variation at field scale rarely simulate irregularity patterns displayed by spatial series of soil properties. The objective of this work was to use CT data to test the hypothesis that soil pore structure at the horizon scale may be represented by multifractal models. X-ray CT scans of twelve, water-saturated, 20-cm long soil columns with diameters of 7.5 cm were analyzed. A reconstruction algorithm was applied to convert the X-ray CT data into a stack of 1480 grayscale digital images with a voxel resolution of 110 microns and a cross-sectional size of 690×690 pixels. The images were binarized and the spatial series of the percentage of void space vs. depth was analyzed to evaluate the applicability of the multifractal model. The series of depth-dependent macroporosity values exhibited a well-defined multifractal structure that was revealed by singularity and Rényi spectra. The long-range dependencies in these series were parameterized by the Hurst exponent. Values of the Hurst exponent close to one were observed indicating the strong persistence in variations of porosity with depth. The multifractal modeling of soil macropore structure can be an efficient method for parameterizing and simulating the vertical spatial heterogeneity of soil pore space.

1. Introduction

The soil pore space arrangement can control important physical and biological processes in soil–plant–microbial systems, where microbial population dynamics, nutrient cycling, diffusion, mass flow and nutrient uptake by roots take place across many orders of magnitude in length scale (Young and Crawford, 2004). A correct statistical model of soil pore structure can be critical for understanding flow and transport processes in soils, creating synthetic soil pore spaces for hypothesis and model testing, and evaluating similarity of pore spaces of different soils.

Heuvelink and Webster, 2001 described complexity as the key word when referring to soil pore space structure. Over the last few decades, the use of fractal geometry for dealing with this complexity has been proposed and fractal techniques have been applied successfully to characterize various aspects of soil pore structure

(eg., Rieu and Sposito, 1991; Bartoli et al., 1991; Perfect and Kay, 1991; Peyton et al., 1994; Anderson and McBratney, 1995; Bird et al., 1996; Crawford and Matsui, 1996; Pachepsky et al., 1996; Gimenez et al., 1997; Baveye et al., 1998).

The fractional Brownian motion was the first type of fractal model that was used to describe the complex behavior of soil spatial variation (Burrough, 1983a,b; Eghball et al., 1999), by using the assumption that the variation of a particular soil property was the realization of a stochastic process. As a particular soil attribute exhibits long-range dependencies associated with the power law decay of the autocorrelation as a function of spacing, soil variability exhibits memory and should be measured via the exponent of the power law or the related Hurst exponent (Burrough, 1983a; Mandelbrot and Van Ness, 1968). A similar research for rocks was demonstrated when both porosity values in well logs of oil reservoirs (Hewett, 1986) and permeability of sedimentary rocks (Makse et al., 1996) displayed long-range spatial autocorrelations. These spatial patterns were of substantial interest for making predictions. The long-range dependency of permeability values implied that the transport of contaminants might be less widely dispersed than predicted by uncorrelated models (Makse et al., 1996).

Fractal models capture the simple fractal behavior that can be described by just one parameter – the fractal dimension – which accounts for scaling properties of the irregular behavior. A closer look at spatial series often showed "bursts" and "jumps" and, in general, types of erratic variation which cannot be explained by simple fractal models. Such complexity may also be found in many distributions in nature which can be described by multifractal structures. These types of complex structures usually emerge as the result of the underlying non-linear dynamics (Falconer, 1990; Peitgen et al., 1992), as realization of stochastic multifractal processes (Riedi et al., 1999), or as superposition of other processes acting simultaneously over a wide range of length scales (Burrough, 1983a). It has been suggested that the variations of soil properties manifest an underlying chaotic, non-linear, dynamic system (Culling, 1988; Phillips, 1993), and therefore highly irregular patterns should be common (Beck and Schlögl, 1995). Multifractal analysis can be used as a tool for investigating the rich structure of such complex patterns. This analysis may add relevant information which can be used to better understand the features of soil variability (Kravchenko et al., 1999; Kravchenko and Pachepsky, 2004; Caniego et al., 2005; Zeleke and Si, 2006).

Valuable information about pore space geometry can be provided by 2-D image analysis of thin soil sections. Multifractal analysis can be used to characterize the heterogeneous 2-D spatial arrangement of solid and void phases (Muller and McCauley, 1992; Posadas et al., 2003; Tarquis et al., 2003; Bird et al., 2006) and the complexity of pore size distribution (Caniego et al., 2001, 2003). These two, a priori, independent aspects can be modeled as mass distributions supported at a domain at a plane or at a size interval, respectively. These distributions can be fully characterized by the spectrum of fractal dimensions.

Recent advance in visualization techniques such as X-ray computed tomography (CT) (e.g., Peyton et al., 1994; Perret et al., 1999; Pierret et al., 2002; Mees et al., 2003) has led to multiple cross-sectional images of the soil sample under study. Cylindrical soil columns were scanned and a large number of images of the sections perpendicular to the axis of the cylinder were obtained, which led to a 3-D structure of soil pore space.

The objective of this work was to test the hypotheses that (a) multifractal modeling was applicable to series of 2-D sectional porosity vs. depth and, (b) a memory exists in those series that can be parameterized.

2. Theory: multifractal analysis and long-range dependency

To characterize the variation of a soil property, it is customary to select a transect and to measure this property at sampling points x_j. Usually, these points are equidistant. In order to observe the scaling behavior of the series μ_j, a set of different meshes with cells or subintervals within the sampling domain is considered. A common choice for mesh generation is dyadic downscaling (Evertsz and Mandelbrot, 1992; Kravchenko et al., 1999). This dyadic downscaling is implemented through the successive partitioning of characteristic sizes $\varepsilon = 2^{-k}L$, where $k = 0,1,2,...$ and L is the length of the column. At each scale ε, a number $N(\varepsilon) = 2^k$ of subintervals $I_i(\varepsilon)$ is obtained. Each subinterval $I_i(\varepsilon)$ determines a stack of contiguous sections x_j with height equal to $\varepsilon = 2^{-k}L$ when $x_j \in I_i(\varepsilon)$. Then, their measures or masses

$$\mu_i(\varepsilon) = \sum_{x_j \in I_i(\varepsilon)} \mu_j / \sum_{x_j} \mu_j$$

are computed from experimental data. This defines the measure or mass distribution μ with $\mu_i(\varepsilon)$ as the measure or the mass of the dyadic subinterval $I_i(\varepsilon)$. The mass $\mu_i(\varepsilon)$ is the fraction of the total pore volume of the column that corresponds to the sections x_j of $I_i(\varepsilon)$. This ratio can be viewed as the contribution of this portion of the column to its total porosity.

The value

$$\alpha_i(\varepsilon) = \frac{\log \mu_i(\varepsilon)}{\log \varepsilon} \tag{1}$$

is the *coarse singularity* or *coarse Hölder exponent* of the *i*-th cell of size ε.

Eq. (1) is equivalent to $\mu_i(\varepsilon) \approx \varepsilon^{\alpha_i(\varepsilon)}$ where "$\approx$" stands for the scaling or asymptotic behavior when ε approaches zero. For most cases the exponent equals one and the measure has a density function. The ratio $\mu_i(\varepsilon)/\varepsilon$ is the empirical density of the subinterval $I_i(\varepsilon)$ and it defines the density function as ε approaches zero and the ratio converges to a non-zero value. In many cases $\mu_i(\varepsilon)/\varepsilon$ diverges or tends towards zero and it is not possible to find a density function. In these cases, the asymptotic behavior of $\mu_i(\varepsilon) / \varepsilon^{\alpha_i(\varepsilon)}$ is well defined when a suitable exponent is chosen but, in general, this exponent varies from one subinterval to another and, eventually, from one point to another as ε approaches zero (Evertsz and Mandelbrot, 1992). These are the singular measures that exhibit a variety of scale dependences. The multifractal analysis aims at studying these singular measures by characterizing the *singularity exponents* α which correspond to the asymptotic behavior of the coarse singular exponents $\alpha_i(\varepsilon)$. These exponents represent the "crowding" or the degree of concentration of μ: the greater this value is, the smaller is the concentration of the measure and vice versa. Typically, singularity exponents α of multi-fractal distributions show a great variability such that their values fill an interval $[\alpha_{min}, \alpha_{max}]$ when ε approaches zero. When this interval reduces to a point it becomes a (mono-)fractal.

Multifractal analysis relies on the idea of grouping together subintervals $I_i(\varepsilon)$ of similar degree of mass concentration α and analyzing the growth rate of the number of subintervals $I_i(\varepsilon)$ as the size ε approaches to zero. Specifically, if $N_\varepsilon(\alpha)$ is the number of subintervals of size ε with singularity exponent between α and $\alpha + \Delta\alpha$, and $f(\alpha)$ is defined by the scaling equation

$$N_\varepsilon(\alpha) \approx \varepsilon^{-f(\alpha)} \text{ for } \varepsilon \to 0,$$

then $f(\alpha)$ converges to a continuous function called the *singularity spectrum* as $\Delta\alpha \to 0$ (Evertsz and Mandelbrot, 1992). If we consider the set A_α of points with a singularity exponent equal to α, $f(\alpha)$ characterizes the tendency of A_α to fill the support of the distribution. As a consequence $f(\alpha)$ may be interpreted as the fractal dimension of A_α. It is worth noting here that the points of each set A_α are spread over the whole interval that is the support of the measure. In this way the mass distribution μ can be characterized through an ensemble of interwoven fractal sets A_α with different fractal dimensions $f(\alpha)$. Within each set A_α the measure displays a particular scaling described by the singularity exponent α.

Following Chhabra and Jensen (1989), the singularity spectrum may be computed using a set of real numbers q by

$$\alpha_q \approx \frac{\sum_{i=1}^{n(\varepsilon)} \mu_i(q,\varepsilon) \log \mu_i(\varepsilon)}{\log \varepsilon} \tag{2}$$

and

$$f(\alpha_q) \approx \frac{\sum_{i=1}^{n(\varepsilon)} \mu_i(q,\varepsilon) \log \mu_i(q,\varepsilon)}{\log \varepsilon} \tag{3}$$

where the quantities $\mu_i(q,\varepsilon)$ are defined as

$$\mu_i(q,\varepsilon) = \frac{\mu_i(\varepsilon)^q}{\sum_{i=1}^{n(\varepsilon)} \mu_i(\varepsilon)^q}.$$

The symbol "$\approx$" stands for the scaling or asymptotic behavior when ε approaches zero and the summation is taken over the $n(\varepsilon)$ cells with no zero mass. Then, the singularity or Hölder exponents as

Fig. 1. View of a 20-cm long soil column with 7.5 cm diameter.

compared to positive values of q which yield low exponents and large concentrations. In particular, α_{max} corresponds to $\alpha(q \to -\infty)$ and α_{min} corresponds to $\alpha(q \to \infty)$. As q varies points $(\alpha_q, f(\alpha_q))$ define a plane curve parameterized by q. It is the singularity spectrum of the measure μ. In general this spectrum has a parabolic shaped concave down graph that attains its maximum value $f(\alpha_0)$ at the point α_0. The singularity exponent α_0 corresponds to the mean value of the singularity exponents α as it is the average of the exponents α weighted by the uniform distribution (Eq. (2)), and $f(\alpha_0)$ gives the box-counting fractal dimension of the support of the measure (Eq. (3)).

Alternatively, the multifractal behavior of a measure μ, with $\mu_i(\varepsilon)$ as measures or masses of the dyadic subintervals $I_i(\varepsilon)$, may be represented using the *Rényi* or *generalized dimensions* that are computed via expressions proposed by Grassberger (1983):

$$D_q \approx \frac{1}{q-1} \frac{\log \sum_{i=1}^{n(\varepsilon)} \mu_i(\varepsilon)^q}{\log \varepsilon} \qquad (4)$$

for $q \neq 1$ and

$$D_1 \approx \frac{\sum_{i=1}^{n(\varepsilon)} \mu_i(\varepsilon) \log \mu_i(\varepsilon)}{\log \varepsilon} \qquad (5)$$

for $q = 1$. Then, the set of points defined by (q, D_q) as q varies, defines a curve that depicts the *Rényi spectrum* of the measure μ. In general, this spectrum is a decreasing function of q with a sigmoidal shape.

The value $D_1 = f(\alpha_1) = \alpha_1$ is the *entropy dimension*. It gauges the scaling behavior of the entropy as the size of the partition ε decreases. We may re-write Eq. (4) as

$$\sum_{i=1}^{n(\varepsilon)} \mu_i(\varepsilon)^q \approx \varepsilon^{(q-1)D_q}. \qquad (6)$$

It follows from Eq. (3) that $D_0 = f(\alpha_0)$ when $q = 0$. This is the *capacity* or box-counting fractal dimension of the support of the measure. In
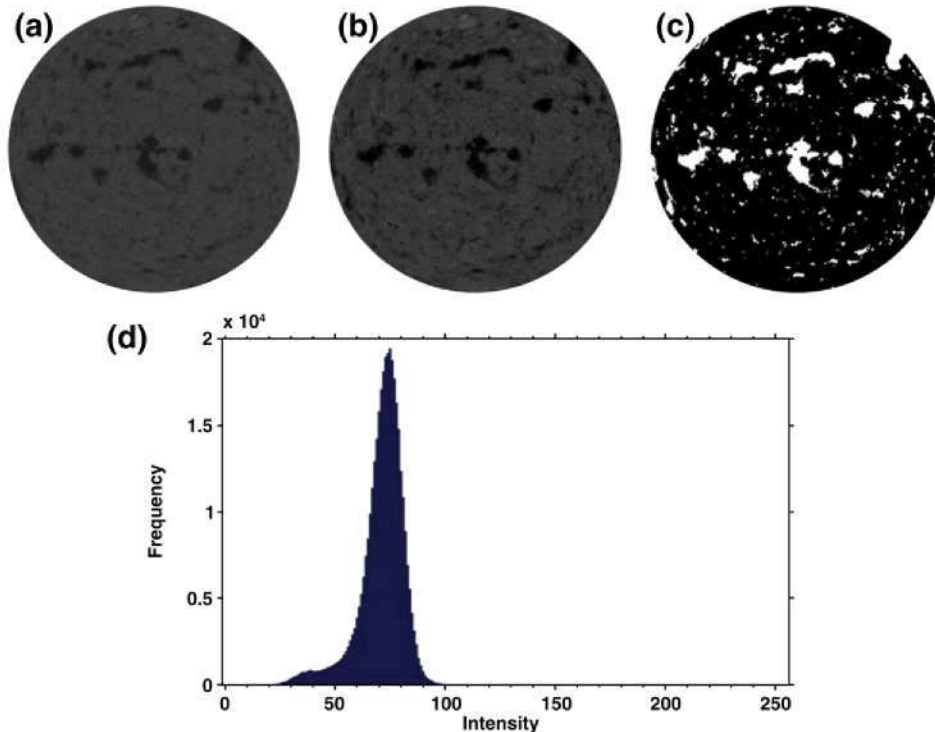
given by Eq. (2) becomes a decreasing function of q. In fact, large values of the parameter q ($q \gg 1$) correspond to small exponents and to high concentrations of the measure. And, small values of the parameter q ($q \ll 1$) correspond to large exponents and to low concentrations of the measure. This is a natural result: in Eq. (2), α_q is obtained as an average with respect to the probability measure defined by quantities $\mu_i(q,\varepsilon)$. These weights magnify the denser (more rarefied) regions for large (small) values of q. Therefore, negative values of q yield high exponents and small concentrations, as

Fig. 2. Illustration of image enhancement and binarization. (a) Original grayscale image; (b) Filtered (enhanced) image; (c) Binarized image; and (d) Grayscale histogram corresponding to the enhanced image depicted in (b).

this case, Eq. (6) determines that cells of size ε with a non-zero mass follow a power law scaling with the exponent D_0. Value of $D_0 = 1$ if all cells of any of considered sizes contain some data and have no zero mass, as long as the size of the partition is not smaller than the separation of two adjacent sections. The value D_2 is the *correlation dimension* (Hentschel and Procaccia, 1983) and captures the scaling behavior of the second sampling moments.

For one-dimensional distributions, the singularity and the Rényi dimensions range from 0 to 1. In the special case of fractional Brownian motions and more general mono-fractals, the singularity spectrum reduces to a point (α, 1) while the Rényi spectrum is a horizontal line: $D(q) = \alpha$. The scaling behavior of (mono-)fractal processes reduces to a single scaling (Riedi et al., 1999).

Now consider μ_j as a stochastic process. For simplicity, we will assume that this is a second order stationary process with a zero mean — i.e. that the first and second moments are stationary. The autocorrelation function is defined as $\rho(k) = E[\mu_{j + k}\mu_j]$ where E stands for the expectation. The process has *memory or long-range dependency* when the autocorrelation function decays with a power law, $\rho(k) \approx k^{2H - 2}$, and $1/2 < H < 1$ (Leland et al., 1994). The parameter H is called the *Hurst exponent* of the process. Then, parameter H characterizes the memory of the stochastic process. For the Brownian motion, the autocorrelation function is constant as these stochastic processes are defined by independent increments. For fractional Brownian motions, the auto-correlation function has the same power law decay and the Hurst exponent coincides with the only multifractal parameter of theirs singularity spectrum.

Since, the correlation dimension D_2 accounts for the scaling behavior of the second sampling moments $\sum_i \mu_i(\varepsilon)^2$ both the Hurst exponent and the correlation dimension measure the power law behavior of the second order statistics. For a large class of multifractal processes the relationship of these parameters can be written as (Riedi et al., 1999):

$$D_2 = 2H - 1$$

This expression provides a way of obtaining the Hurst exponent to analyze the memory of general multifractal processes. The classical methods of estimating the Hurst exponent work only for mono-fractal processes as fractional Brownian motions, whose scaling behavior may be described by a single exponent (Burrough, 1983a; Hewett, 1986). As a result, multifractal analysis, which goes beyond second order statistics, provides an effective way to determine and quantify the memory of general multifractal stochastic processes.

3. Materials and methods

3.1. Sampling

Twelve undisturbed cylindrical soil columns of 7.5 cm diameter and 20 cm height (Fig. 1) were collected vertically from a well-structured A horizon of a Tyler soil, fine-silty, mixed, mesic, Aeric Fragiaquults (Soil Survey Staff, 1999) from a 1-m^2 plot. The experimental area was a floodplain grazing site in Franklin County, Pennsylvania, USA. The Uhland type core sampler cutting head (Uhland, 1949) with an acrylic cylinder was used to obtain the soil columns within the upper 25 cm of the A horizon. The top 2–3 cm soil layer was removed before soil sampling. A soil cylinder approximately 100 mm in diameter and a height of 2–3 cm was cut around the sampler cutting head and the sampler was pressed into the soil. Then the soil was cleaned around the sampler and the sampling procedure repeated until the cutting head approached the depth of 25 cm. This sampling procedure provided gradual penetration of the sampler into the soil with minimum disturbance of the soil core. The soil core was removed from the sampler and soil protruding from the top and bottom of the acrylic cylinder was cut. The soil core was wrapped with cling wrap and aluminum foil, and kept at 10 °C.

The soil contained on average 26% of clay, 46% of silt and 28% of sand. The organic matter content was 3.3%. The dry aggregate size distribution was determined by sieving into the following aggregate diameter groups: <0.063, 0.063–0.125, 0.125–0.25, 0.25–0.5, 0.5–2, 2–4 and >4 mm. Mass fractions of the aggregate groups were 2.19 ± 0.75, 1.22 ± 0.44, 1.82 ± 0.52, 2.86 ± 0.70, 18.0 ± 3.4, 27.5 ± 4.2 and $46.4 \pm 8.1\%$ respectively. The soil was well-structured as aggregates larger than 2-mm constituted on average 74% of total solid mass.

3.2. X-ray tomography of soil columns

The industrial scanner used for this study was a HYTEC Flat Panel Amorphous Silicon High-Resolution Computed Tomography (FLASHCT™) system located at Washington State University. The FLASHCT™ was an advanced high-speed industrial X-ray based 3-D scanning system, developed as an area detector scanner employing flat panel amorphous silicon arrays. FLASHCT™ is suitable for applications requiring a wide spectrum of X-ray energies and geometric magnifications. The scanner incorporated both a 225 keV micro-focus X-ray source for material characterization at high magnification and a 420 keV X-ray source for larger component analysis.
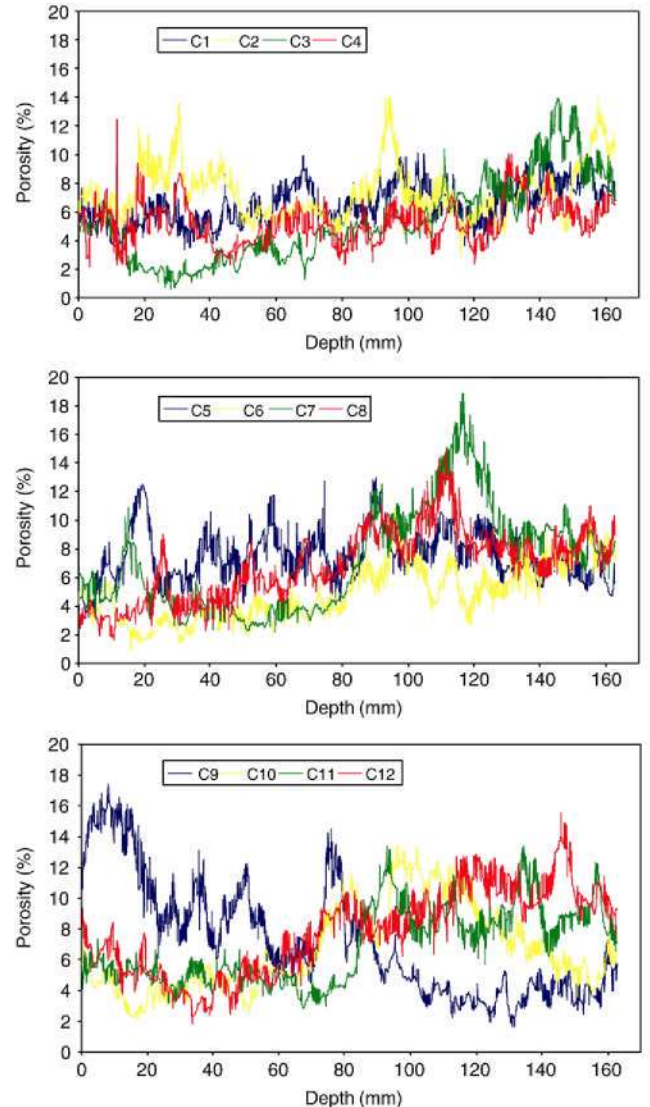

Fig. 3. Series of sectional porosity values (%) as function of depth (mm) of soil columns.

Because the samples slightly detached from the polycarbonate cylinders during transport and storage they were slowly saturated from the bottom with tap water. After mounting the columns onto the rotation stage, they were scanned at an energy level of 380 keV and 1.7 mA current with copper filters positioned between the X-ray source and the columns. A cone beam reconstruction algorithm was applied to convert the X-Ray CT radiographs into 8-bit, grayscale 3-D volumes comprised of $820 \times 820 \times 1480$ voxels (resolution = 110 μm). Note that cone beam reconstruction was not able to capture the end portions of the scanned columns because information from preceding and succeeding portions was needed. Hence, only the center (1480 voxels = 16.28 cm length) was reconstructed. For subsequent analysis, grayscale data were saved in uncompressed Tag Image File Format (TIFF).

3.3. Image processing

Before processing, the TIFF images were cropped with a circular mask to eliminate all portions that were not part of the sample (i.e. polycarbonate cylinder in Fig. 1). This yielded cross-sections of about 690×690 voxels. Because the extruded polycarbonate cylinders were not perfectly round, it was impossible to accurately center samples of this size on the scanner's rotation stage. There was a slight deviation between the nominal inner diameter (7.50 cm) and the image-derived

diameter (7.56 cm). After cropping, median and Fourier band-pass filters coded in MATLAB® (version R2007) were applied for image enhancement to minimize ring-noise artifacts introduced during the scanning process. The median filter replaced the grayscale value of a pixel with the median grayscale of neighboring pixels, thereby minimizing noise while preserving contrast. Fourier filtering was based on the frequency components of the image signal. The signal was transformed into the frequency domain where user-specified bands of the frequency spectrum were removed before inverse transforming the modified spectrum back to the spatial domain. Band-pass filters remove a portion of the frequency spectrum (band) based on user-specified upper and lower cutoff frequencies. We used a low-pass filter with the normalized cutoff frequency set to 0.25 (original and enhanced images shown in Fig. 2a and b).

The transformation of the cropped grayscale to binary images was accomplished with a simple histogram shape-based thresholding technique. Due to the relatively smooth and distinctively bimodal image histograms we chose a method originally developed by Zack et al. (1977), which first identifies the histogram peak representing the light background – solid phase – pixel cluster, and then connects this peak with the first pin of the grayscale histogram that contains dark – void – pixels through a straight line. An algorithm was then applied to find the maximum normal distance between the connecting line and the histogram. The gray level that corresponded to the
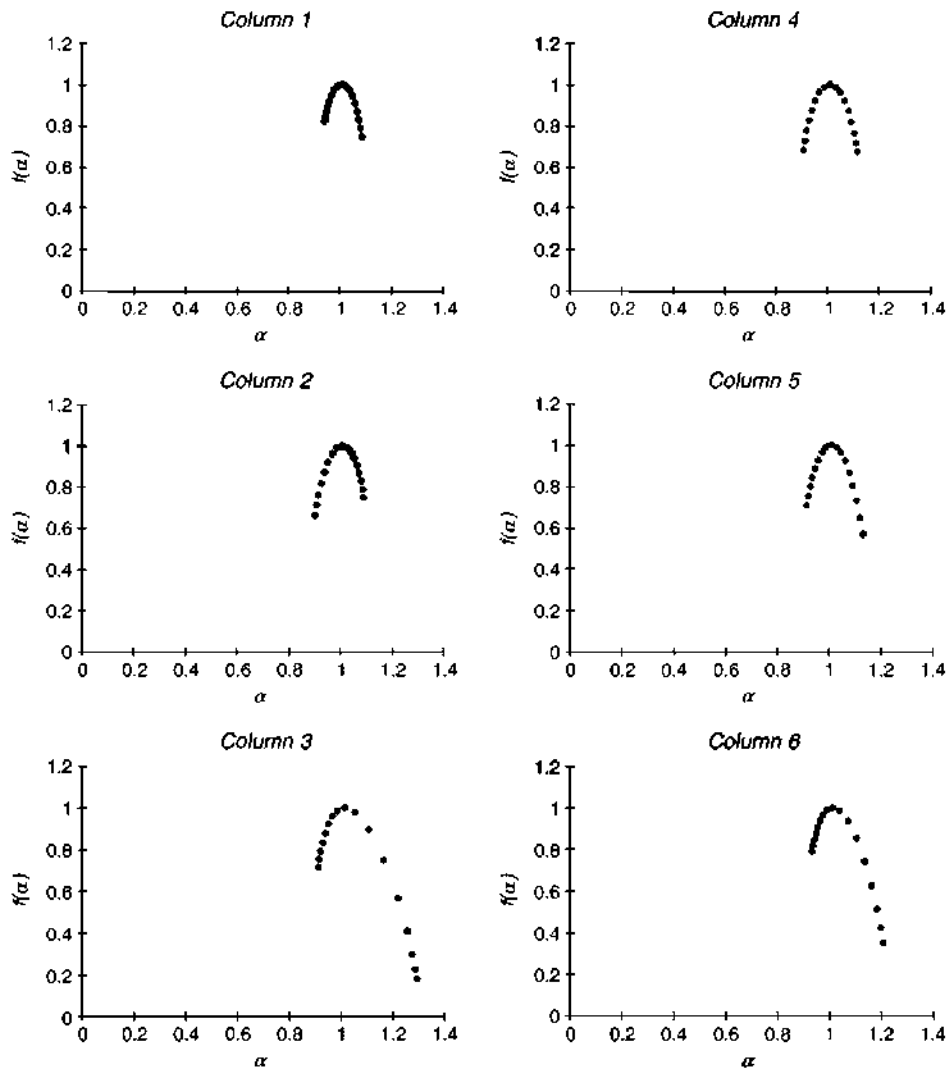

Fig. 4. Singularity spectra of columns #1 to #6.

maximum distance was then selected as the binarization threshold (Tsai and Lee, 2002). As discussed in Rosin (2001), the applied triangulation method worked exceptionally well for histograms with a prominent high, and less developed low intensity peak. CT data were binarized in 2-D "slice-by-slice". The maximum deviation between the thresholds of the 1480 slices was 4 gray levels. Fig. 2d and c represented the grayscale histogram and binarized images. The binarization algorithm was coded in MATLAB® (version R2007).

Matrox® Inspector v.4.1 (Matrox Electronic Systems Ltd.) was used to describe the porosity for each of the 2-D sectional binarized images (San José Martínez et al., 2007). It was assumed that single pixel objects were artifacts of the imaging process (Hatano et al., 1992; VandenBygaart and Protz, 1999) and only voids with more than four connected pixels were considered, which corresponds to macropores with an equivalent diameter of 0.78 mm.

3.4. Estimation of multifractal parameters

For each column we determined the series of μ_j values corresponding to the percentage of void space of the j-th sectional binarized image. These series were used to estimate the multifractal parameters through the quantities $\mu_j(\varepsilon)$ as described in Section 2. When analyzing the measure μ, successive dyadic partitions of the length of the column L, were used. At the first level we had two subintervals each one

containing one half of the quantities μ_j, at the second level we had four subintervals each one containing one fourth of these quantities, etc. The smallest partition was chosen so that all its subintervals contained at least one of the quantities μ_j. The μ_j sectional porosity value was 1480 for each column, ε varied between 2^{-1} and 2^{-10} the size of the vertical length of the column. The parameter q of expressions (2), (3), (4) and (5) was chosen between -8 and 8 in increments of 1; hence, we considered 17 possible scalings following standards when implementing multifractals analysis in soil sciences (Muller and McCauley, 1992; Kravchenko et al., 1999; Zeleke and Si, 2006). The multifractal structure of soil pore variation was determined by means of three sets of multifractal parameters, namely, the singularity exponents α_q (Eq. (2)), their associated fractal dimensions $f(\alpha_q)$ (Eq. (3)) and the Rényi generalized dimensions D_q (Eqs. (4) and (5)) (Caniego et al. 2001, 2003). They were estimated via linear regression analysis with the least mean-square fit applying the power laws given in expressions (2), (3), (4) and (5). Coefficients of determination R^2 and standard errors SE of the slope of the regression line were recorded. Probability distribution functions of R^2 and SE were characterized by quartiles.

4. Results and discussion

The series of depth-dependent porosity values determined for the twelve columns (Fig. 3) exhibited a fully developed multifractal
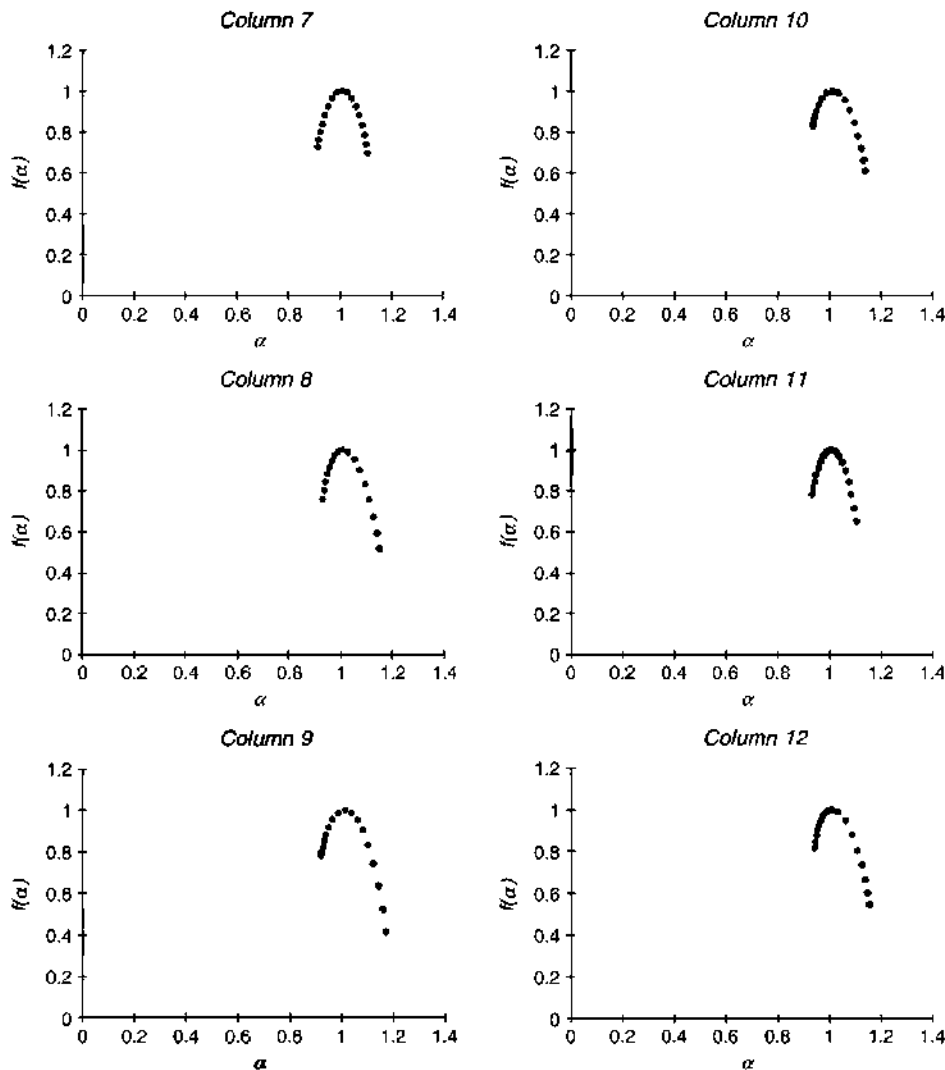

Fig. 5. Singularity spectra of columns #7 to #12.

structure that could be represented by three sets of multifractal parameters: α_q, $f(\alpha_q)$, and D_q. Figs. 4 and 5 depict the singularity spectra while Figs. 6 and 7 correspond to the Rényi spectra. Quartiles of distributions of the coefficients of determination R^2 and the standard errors of the slope of the regression line SE of the estimate of the multifractal parameters α_q, $f(\alpha_q)$, and D_q revealed in Tables 1-3, respectively. Values of R^2 less than 0.9 in columns #3 and #6 correspond to extreme values on the right of the singularity spectrum $f(\alpha_q)$. The results suggest that the variation of the sectional porosities of these columns cannot be explained by using fractional Brownian motions because in all cases, the porosity series display a rich variety of different scalings as expressed by the variation of multifractal parameters with different values of q.

The shape of the singularity spectrum revealed several features of the complex behavior detected by multifractal parameters. The singularity spectrum usually displayed a parabolic shaped concave graph that attained its maximum at α_0, with $f(\alpha_0) = D_0$. The width of the spectrum $\alpha_{max} - \alpha_{min}$ may be related to the heterogeneity of the series; that is, the wider the spectrum, the greater the variety of scalings of the studied series and vice versa. We observed that these values were quite similar among columns (Fig. 8) indicating a similar degree of heterogeneity. Column #3 was an exception to this behavior that could be related to the fact that the extreme values on the left of the spectrum were less accurate in this case. This could also explain the rather high value of this parameter for column #6.

Another feature of the spectra shapes was the symmetry with respect to the vertical line that goes through the maximum spectrum value (α_0, D_0). This can be assessed by using two parameters. Firstly, we considered $R - L = (\alpha_{max} - \alpha_0) - (\alpha_0 - \alpha_{min})$ which measures the symmetry in the horizontal axis of the range $[\alpha_{min}, \alpha_{max}]$ with respect to α_0. When this value was zero, the range $[\alpha_{min}, \alpha_{max}]$ was symmetrical with respect to α_0 and the scaling exponents α were spread equally on both sides of $[\alpha_{min}, \alpha_{max}]$. The value $V = f(\alpha_{min}) - f(\alpha_{max})$ expressed the vertical difference between the two branches of the spectrum. Fig. 9 summarized the estimates of these two parameters. It suggested that columns #4 and #7 had a symmetrical singularity spectrum, while only column #2 had an asymmetric spectrum with a longer but narrower left branch and the other nine columns showed the same type of asymmetry but with a longer but narrower right branch.

The shape of the most common spectra pattern corresponding to columns #1, #3, #5, #6, #8, #9, #10, #11 and #12 indicated that larger concentrations are less diverse and more common than smaller concentrations. Specifically, in these cases, the right branch of the spectrum was wider as $R - L > 0$ (see Fig. 9). This manifested a greater variety of the highest singularity exponents α which corresponded to low concentrations (Eq. (1)) and to negative values of q (Eq. (2)). This right branch was also longer as $V > 0$ (see Fig. 9). This meant that the geometrical size of points with the largest exponents α was smaller. The left branch of the spectrum was narrower, which indicated a lesser variety of the smallest singularity exponents α which correspond to
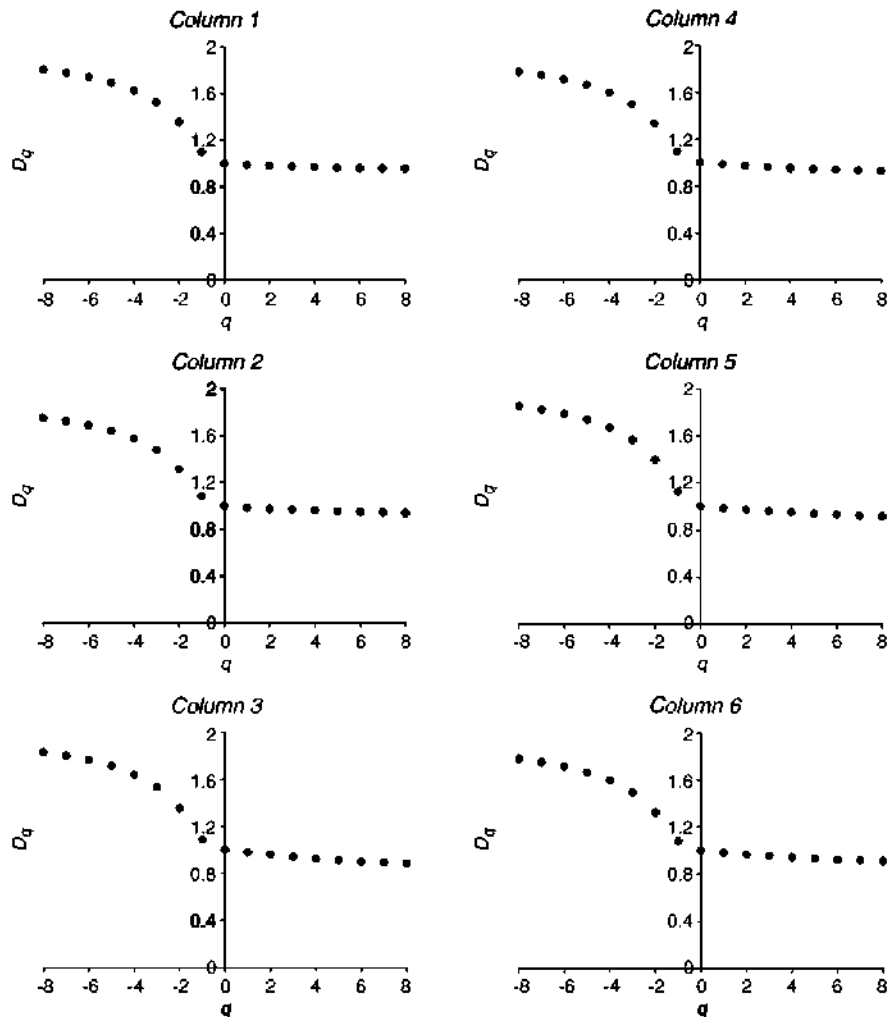

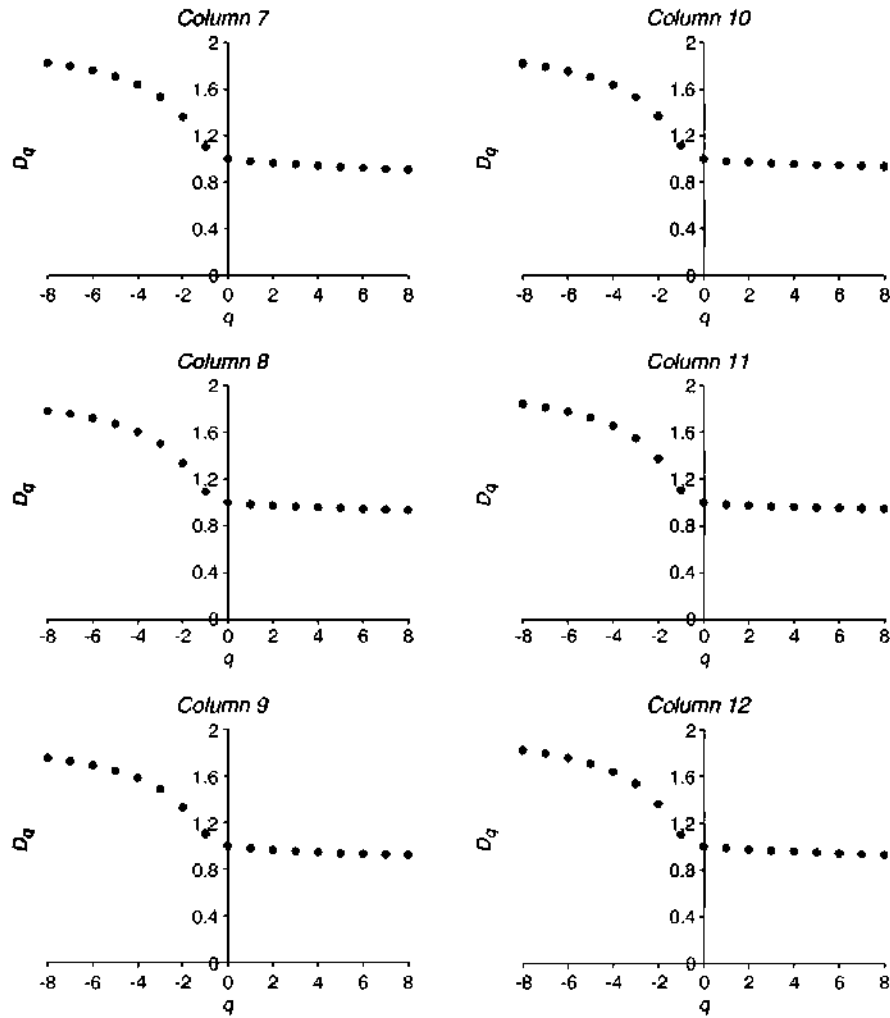Fig. 6. Rényi spectra of columns #1 to #6.

Fig. 7. Rényi spectra of columns #7 to #12.

high concentrations (Eq. (1)) and to positive values of q (Eq. (2)). The left branch was also shorter, which meant that the geometrical size of points with the smallest exponents α was larger. In terms of the series of porosity values as a function of depth, it suggested that the highest porosity values dominated along the column height and that these high concentrations were quite similar to each other as compared to the lowest porosity values that were not as common and exhibited more differences between one another along the column height. Our results also indicated that this is the general pattern observed in the sampled columns. Columns #4 and #7 had quite balanced distributions of the lowest and the highest concentrations.

Only column #2 displayed the behavior opposite to that described above. For this column, we observed that low porosities dominated along the column height but that these low concentrations were quite similar to each other while high porosities were not so common but were more different from one another along the column height. The column #2 spectrum was not as far from symmetry as spectra of the other columns (Fig. 9).

Table 1

Summary of the goodness of fit statistics of standard errors SE and coefficients of determination R^2 for the estimation of singularity exponents α_q.

Column	Quartile 0		Quartile 1		Quartile 2		Quartile 3		Quartile 4	
	SE	R^2	SE	R^2	SE	R^2	SE	R^2	SE	R^2
1	0.0024	0.9986	0.0090	0.9988	0.0115	0.9989	0.0127	0.9993	0.0143	>0.9999
2	0.0022	0.9990	0.0081	0.9992	0.0100	0.9993	0.0101	0.9994	0.0106	>0.9999
3	0.0023	0.9944	0.0093	0.9958	0.0138	0.9983	0.0281	0.9992	0.0339	>0.9999
4	0.0023	0.9985	0.0086	0.9988	0.0107	0.9990	0.0126	0.9994	0.0155	>0.9999
5	0.0023	0.9987	0.0087	0.9989	0.0109	0.9990	0.0120	0.9993	0.0145	>0.9999
6	0.0022	0.9949	0.0087	0.9976	0.0113	0.9988	0.0199	0.9994	0.0305	>0.9999
7	0.0022	0.9984	0.0085	0.9991	0.0097	0.9994	0.0101	0.9995	0.0130	>0.9999
8	0.0023	0.9963	0.0089	0.9981	0.0110	0.9989	0.0171	0.9993	0.0248	>0.9999
9	0.0021	0.9980	0.0084	0.9989	0.0103	0.9993	0.0124	0.9995	0.0144	>0.9999
10	0.0022	0.9985	0.0084	0.9990	0.0108	0.9992	0.0118	0.9995	0.0127	>0.9999
11	0.0024	0.9987	0.0092	0.9990	0.0115	0.9991	0.0117	0.9993	0.0119	>0.9999
12	0.0022	0.9988	0.0090	0.9990	0.0115	0.9991	0.0118	0.9994	0.0121	>0.9999

Table 2
Summary of the goodness of fit statistics of standard errors SE and coefficients of determination R^2 for the estimation of fractal dimensions $f(\alpha_q)$.

Column	Quartile 0		Quartile 1		Quartile 2		Quartile 3		Quartile 4	
	SE	R^2	SE	R^2	SE	R^2	SE	R^2	SE	R^2
1	<0.0001	0.9771	0.0082	0.9927	0.0198	0.9962	0.0256	0.9994	0.0405	>0.9999
2	<0.0001	0.9849	0.0075	0.9931	0.0141	0.9979	0.0224	0.9995	0.0327	>0.9999
3	<0.0001	0.3064	0.0128	0.9044	0.0334	0.9860	0.0652	0.9984	0.0998	>0.9999
4	<0.0001	0.9717	0.0079	0.9913	0.0187	0.9964	0.0253	0.9995	0.0406	>0.9999
5	<0.0001	0.9614	0.0079	0.9912	0.0185	0.9963	0.0243	0.9995	0.0401	>0.9999
6	<0.0001	0.6332	0.0083	0.9813	0.0232	0.9944	0.0363	0.9994	0.0941	>0.9999
7	<0.0001	0.9741	0.0076	0.9906	0.0141	0.9978	0.0261	0.9995	0.0418	>0.9999
8	<0.0001	0.8582	0.0081	0.9913	0.0219	0.9948	0.0275	0.9994	0.0743	>0.9999
9	<0.0001	0.8278	0.0077	0.9796	0.0226	0.9948	0.0374	0.9995	0.0662	>0.9999
10	<0.0001	0.9684	0.0080	0.9907	0.0179	0.9958	0.0293	0.9994	0.0388	>0.9999
11	<0.0001	0.9555	0.0084	0.9914	0.0185	0.9962	0.0268	0.9994	0.0495	>0.9999
12	<0.0001	0.9776	0.0081	0.9921	0.0195	0.9960	0.0259	0.9994	0.0292	>0.9999

Table 3
Summary of the goodness of fit statistics of standard errors SE and coefficients of determination R^2 for the estimation of Rényi dimensions D_q.

Column	Quartile 0		Quartile 1		Quartile 2		Quartile 3		Quartile 4	
	SE	R^2	SE	R^2	SE	R^2	SE	R^2	SE	R^2
1	<0.0001	0.9992	0.0118	0.9995	0.0439	0.9995	0.0670	0.9997	0.1306	0.9999
2	<0.0001	0.9984	0.0132	0.9985	0.0459	0.9992	0.1090	0.9996	0.2215	0.9999
3	<0.0001	0.9957	0.0196	0.9978	0.0894	0.9979	0.1443	0.9991	0.2694	0.9999
4	<0.0001	0.9991	0.0128	0.9992	0.0455	0.9993	0.0803	0.9996	0.1634	0.9999
5	<0.0001	0.9992	0.0115	0.9995	0.0389	0.9996	0.0637	0.9998	0.1320	0.9999
6	<0.0001	0.9988	0.0129	0.9989	0.0477	0.9991	0.0944	0.9996	0.1850	0.9999
7	<0.0001	0.9981	0.0193	0.9988	0.0502	0.9995	0.0825	0.9997	0.1263	0.9999
8	<0.0001	0.9993	0.0126	0.9996	0.0334	0.9997	0.0610	0.9998	0.1023	0.9999
9	<0.0001	0.9974	0.0195	0.9984	0.0747	0.9985	0.1163	0.9992	0.2224	0.9999
10	<0.0001	0.9985	0.0194	0.9987	0.0435	0.9994	0.1058	0.9995	0.2233	0.9999
11	<0.0001	0.9989	0.0145	0.9994	0.0503	0.9994	0.0777	0.9995	0.1437	0.9999
12	<0.0001	0.9989	0.0128	0.9994	0.0479	0.9994	0.0763	0.9996	0.1431	0.9999

The Rényi spectra (Figs. 6 and 7) were more similar to each other than singularity spectra. They displayed a noticeable variation across negative values of q. This branch of the spectrum corresponded to the smallest concentrations of the measure (Caniego et al., 2003). This was in agreement with the observation that in general the singularity spectra had a more developed right branch.

The values of the Hurst exponents were 0.9896, 0.9867, 0.9797, 0.9858, 0.9860, 0.9828, 0.9823, 0.9867, 0.9828, 0.9850, 0.9865 and 0.9866 for columns one to twelve, respectively. These were very close to one and quite similar to one another. These values reflected the presence of strong persistence or positive autocorrelations (Norouzzadeh et al., 2007) occurring in case of long-range dependencies. These correlation dependencies were also common in mono-fractal models such as the fractional Brownian motion model with Hurst exponents between one half and one (Riedi et al., 1999).

The similarities detected between the multifractal parameters for the twelve columns — especially with regard to spectra-shape and Hurst exponents — reflected the low spatial variability of soil properties in horizontal directions as a consequence of the relatively small size (1 m^2) of the plot were the columns were extracted.

Our results suggested that the variation of soil porosity as depth increases displays a complex scaling behavior with a similar structure in vertical direction at the horizon scale. Within a square-meter plot, we were likely to find that high porosities dominating in studied soil
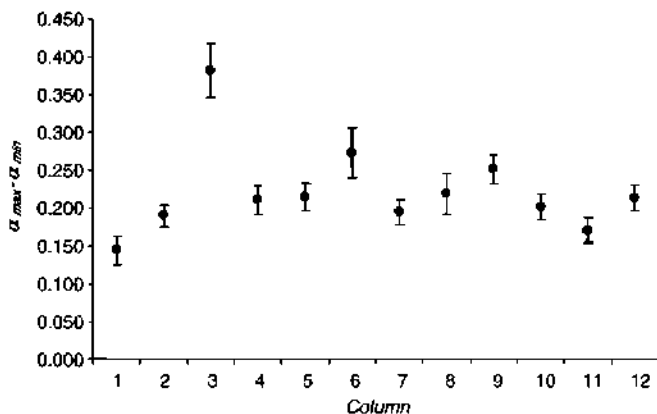

Fig. 8. Width of $|\alpha_{min}, \alpha_{max}|$ as measured by $\alpha_{max}-\alpha_{min}$ where values of α_{max} and α_{min} are approximated by α_{-8} and α_8, respectively. Errors bars correspond to one SE.
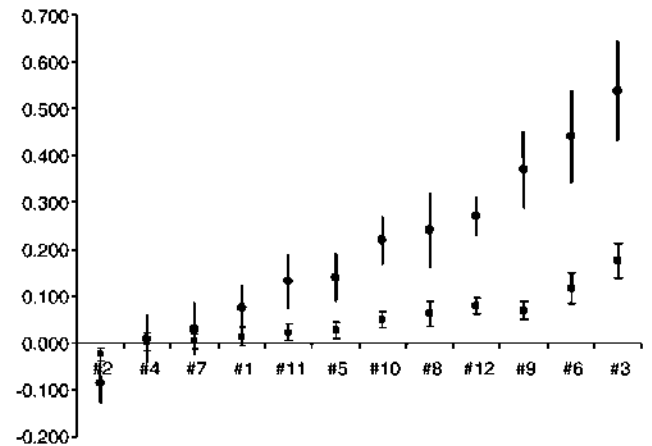

Fig. 9. Symmetry of the singularity spectra as measured by $R-L = (\alpha_{max}-\alpha_0)-(\alpha_0-\alpha_{min})$ (●) and $V = f(\alpha_{min})-f(\alpha_{max})$ (■) for the twelve soil columns. The values of α_{max} and α_{min} are approximated by α_{-8} and α_8, respectively. Columns are ordered by increasing values of $f(\alpha_{min})-f(\alpha_{max})$. Error bars correspond to one SE.

horizon, and that these high concentrations were quite similar to each other. These findings are consistent with previous studies on the multifractal patterns of the spatial variability of various soil attributes at field scale (Kravchenko et al., 1999; Kravchenko and Pachepsky, 2004; Caniego et al., 2005; Zeleke and Si, 2006). Moreover, the analysis of the memory of the variation with depth indicated that a rather strong persistence rules the variation at the plot scale as was suggested by the high values of the Hurst exponent. This fact was consistent with the previous work of Hewett (1986), and Hewett and Behrens (1988) that studied the heterogeneity of oil reservoirs showed similar results at a different scale for the vertical variation of porosity.

In the context of the investigations of flow processes in soil (Sahimi, 1993; Perfect and Sukop, 2001), one of the most challenging problems was related to the prediction of flow phenomena features from pore geometrical characteristics. One question of interest for the future study could be the degree of correlation between hydraulic conductivity parameters and the Hurst exponent measuring the memory of the series of soil porosity sections.

5. Conclusions

We performed the multifractal analysis of a series of depth-dependent macroporosity values of twelve undisturbed soil columns. The series corresponded to the percentage of void space of the sectional binarized images of 1480, 8-bit, grayscale images from X-ray CT radiographs with a voxel resolution of 110 μm. These series exhibited a fully developed multifractal structure that was represented by three sets of multifractal parameters, namely, the singularity exponents α_q, their associated fractal dimensions $f(\alpha_q)$ and the Rényi generalized dimensions D_q, estimated by linear regression analysis. The singularity $f(\alpha)$ and the Rényi D_q spectra obtained were consistent with multifractal measures where larger concentrations were less diverse but more common than the smaller ones. Moreover, the values of Hurst exponents H were quite close to one and similar among the studied soil columns. These values reflected the presence of rather strong persistence or positive autocorrelations also termed long-range dependencies.

Our results are of interest for modeling and simulating soil pore spatial geometry and associated fluid flow phenomena. Multifractal patterns exhibited by soil porosity series of the collected columns suggested the need for multifractal geometrical models of the structure of soil porosity. These models should account for a multifractal random structure compatible with the multinomial structure and the long-range dependences that displayed these porosity series as shown by our analysis.

References

Anderson, A.N., McBratney, A.B., 1995. Soil aggregates as mass fractals. Aust. J. Soil Res. 33, 757–772.

Bartoli, F., Philippy, R., Doirisse, M., Niquet, S., Dubuit, M., 1991. Structure and self-similarity in silty and sandy soils: the fractal approach. J. Soil Sci. 42, 167–185.

Baveye, P., Parlange, J.Y., Stewart, B.A. (Eds.), 1998. Fractals in Soil Sciences. CRC Press, Boca Raton, Fla. USA, p. 377.

Beck, C., Schlögl, F., 1995. Thermodynamics of Chaotic Systems. An Introduction. Cambridge University Press, New York.

Bird, N.R.A., Bartoli, F., Dexter, A.R., 1996. Water retention models for fractal soil structures. Eur. J. Soil Sci. 47, 1–6.

Bird, N., Díaz, M.C., Saa, A., Tarquis, A.M., 2006. Fractal and multifractal analysis of pore-scale images of soil. J. Hydrol. 322, 211–219.

Burrough, P.A., 1983a. Multiscale sources of spatial variation in soil I. The application of fractal concepts to nested levels of soil variation. J. Soil Sci. 34, 577–597.

Burrough, P.A., 1983b. Multiscale sources of spatial variation in soil II. A non-Brownian fractal model and its application in soil survey. J. Soil Sci. 34, 599–620.

Caniego, F.J., Martín, M.A., San José, F., 2001. Singularity features of pore size distribution: singularity strength analysis and entropy spectrum. Fractals 2001 (6), 305–316.

Caniego, F.J., Martín, M.A., San José, F., 2003. Rényi dimensions of soil pore size distribution. Geoderma 112, 205–216.

Caniego, F.J., Espejo, R., Martín, M.A., San José, F., 2005. Multifractal scaling of soil spatial variability. Ecol. Model. 182, 291–303.

Chhabra, A., Jensen, V.J., 1989. Direct determination of the $f(\alpha)$ singularity spectrum. Phys. Rev. Lett. 62, 1327–1330.

Crawford, J.W., Matsui, N., 1996. Heterogeneity of the pore and solid volume of soil: distinguishing a fractal space from its nonfractal complement. Geoderma 73, 183–195.

Culling, W.E.H., 1988. Dimension entropy in the soil-covered landscape. Earth Surf. Process. Landf. 13, 619–648.

Eghball, B., Hergert, G.W., Lesoing, G.W., Ferguson, R.B., 1999. Fractal analysis of spatial and temporal variability. Geoderma 88, 349–362.

Evertsz, C.J.G., Mandelbrot, B.B., 1992. Multifractal measures. In: Peitgen, H., Jürgens, H., Saupe, D. (Eds.), Chaos and Fractals. Springer, Berlin, pp. 921–953.

Falconer, K., 1990. Fractal geometry. Mathematical Foundations and Applications. John Wiley & Sons, Chichester.

Gimenez, D., Perfect, E., Rawls, W.J., Pachepsky, Ya., 1997. Fractal models for predicting soil hydraulic properties: a review. Eng. Geol. 48, 161–183.

Grassberger, P., 1983. Generalized dimensions of strange attractors. Phys. Lett. 97A, 227–230.

Hatano, R., Kawamura, N., Ikeda, J., Sakuma, T., 1992. Evaluation of the effect of morphological features of flow paths on solute transport by using fractal dimensions of methylene blue staining pattern. Geoderma 53, 31–44.

Hentschel, H.G.E., Procaccia, I., 1983. The infinite number of generalized dimensions of fractals and strange attractors. Physica, D 8, 435–444.

Heuvelink, G.B.M., Webster, R., 2001. Modeling soil variation: past, present and future. Geoderma 100, 269–301.

Hewett, T.A., 1986. Fractal distribution of reservoir heterogeneity and their influence in fluid transport. Paper SPE 15386 presented at 1986 Annual Technical Conference and Exhibition, New Orleans, October 5–8.

Hewett, T.A., Behrens, R.A., 1988. Condition simulation of reservoir heterogeneity with fractals. Paper SPE 18326 presented at 1988 Annual Technical Conference and Exhibition, Houston, October 2–5.

Kravchenko, A.N., Pachepsky, Y.A., 2004. Fractal techniques to assess spatial variability in soil processes. In: Álvarez-Benedí, J., Munóz-Carpena, R. (Eds.), Soil–Water–Solute Process Characterization: An Integrated Approach. CRC Press, Boca Raton, FL, USA, pp. 617–638.

Kravchenko, A.N., Boast, C.W., Bullock, D.G., 1999. Multifractal analysis of soil spatial variability. Agron. J. 91, 1033–1041.

Leland, W.E., Taqqu, M.S., Willinger, W., Wilson, W., 1994. On the self-similar nature of ethernet traffic (extended version). IEEE Trans. Netw. 2, 1–15.

Mandelbrot, B.B., Van Ness, J.W., 1968. Fractional Brownian motions, fractional noises and applications. SIAM Rev. 10, 422–437.

Makse, H.A., Havlin, S., Ivanov, P.Ch., King, P.R., Prakash, S., Stanley, H.E., 1996. Pattern formation in sedimentary rocks: connectivity, permeability, and spatial correlations. Physica, A 233, 587–605.

Mees, F., Swennen, R., van Geet, M., Jacobs, P. (Eds.), 2003. Applications of X-ray computed tomography in geosciences: Geological Society, London, Special publication, vol. 215, p. 243.

Muller, J., McCauley, J.L., 1992. Implication of fractal geometry for fluid flow properties of sedimentary rocks. Transp. Porous Media 8, 133–147.

Norouzzadeh, P., Dullaertc, W., Rahmanid, B., 2007. Anti-correlation and multifractal features of Spain electricity spot market. Physica A 380, 333–342.

Peitgen, H., Jürgens, H., Saupe, D., 1992. Chaos and Fractals. Springer, New York.

Pachepsky, Y.A., Yakovchenko, V., Rabenhorst, M.C., Pooley, C., Sikora, L., 1996. Fractal parameters of pore surface as derived from micromorphological data: etrect of long-term management practices. Geoderma 74, 305–320.

Perfect, E., Kay, B.D., 1991. Fractal theory applied to soil aggregation. Soil Sci. Sot. Am. J. 55, 1552–1558.

Perfect, E., Sukop, M.C., 2001. Models relating solute dispersion to pore space geometry in saturated media: A review. In: Selim, H.M., Sparks, D.L. (Eds.), Physical and chemical processes of water and solute transport/retention in soils. : SSSA Special Publ., vol. 56. SSSA, Madison WI, pp. 77–146.

Perret, J., Prasher, S.O., Kantzas, A., Langford, C., 1999. Three-dimensional quantification of macropore networks in undisturbed soil cores. Soil Sci. Soc. Am. J. 63, 1530–1543.

Pierret, A., Capowiez, Y., Belzunces, L., Moran, C.J., 2002. 3D reconstruction and quantification of macropores using x-ray computed tomography and image analysis. Geoderma 106, 247–271.

Peyton, R.L., Gantzer, C.J., Anderson, S.H., Haeffner, B.A., Pfeifer, P., 1994. Fractal dimension to describe soil macropore structure using X-ray computed tomography. Water Resour. Res. 30, 691–700.

Phillips, J.D., 1993. Stability implications of the state factor model of soils as a nonlinear dynamical system. Geoderma 58, 1–15.

Posadas, A.N.D., Giménez, D., Quiroz, R., Protz, R., 2003. Multifractal characterization of soil pore systems. Soil Sci. Soc. Am. J. 67, 1361–1369.

Riedi, R.H., Crouse, S., Ribeiro, V.J., Baraniuk, R.G., 1999. A multifractal wavelet model with application to network traffic. IEEE Trans. Inf. Theory 45, 992–1019.

Rieu, M., Sposito, G., 1991. Fractal fragmentation, soil porosity and soil water properties: I. Theory. Soil Sci. Sot. Am. J 55, 1231–1238.

Rosin, P.L., 2001. Unimodal thresholding. Pattern Recogn. 34, 2083–2096.

Sahimi, M., 1993. Flow phenomena in rocks: from continuum models to fractals, percolation, cellular automata, and simulated annealing. Rev. Mod. Phys. 65, 1393–1534.

San José Martínez, F., Caniego, F.J., García-Gutiérrez, C., Espejo, R., 2007. Representative elementary area for multifractal analysis of soil porosity using entropy dimension. Nonlinear Process. Geophys. 14, 503–511.

Soil Survey Staff, 1999. A Basic System of Soil Classification for Making and Interpreting Soil Surveys. Second Edition. United States Department of Agriculture. Natural Resources Conservation Service. Agriculture Handbook Number 436. U.S. Government Printing Office, Washington, DC 20402.

Tarquis, A.M., Giménez, D., Saa, A., Díaz, M.C., Gascó, J.M., 2003. Scalings and multiscalings of soil pore systems determine by image analysis. In: Pachepsky, Y., Radcliffe, D.E., Selim, H.M. (Eds.), Scalings Methods in Soil Physics. CRC Press, Boca Raton, Florida, USA, pp. 19–33.

Tsai, C.M., Lee, H.J., 2002. Binarization of color document images via luminescence and saturation color features. IEEE Trans. Image Process. 11, 434–451.

Uhland, R.E., 1949. Physical properties of soils as modified by crops and management. Soil Science Society of America Proceedings 14, 361–366.

VandenBygaart, A.J., Protz, R., 1999. The representative elementary area_REA/in Studies of quantitative soil micromorphology. Geoderma 89, 333–346.

Young, I.M., Crawford, J.W., 2004. Interactions and self-organization in the soil–microbe complex. Science 304 (5677).

Zack, G.W., Rogers, W.E., Latt, S.A., 1977. Automatic measurement of sister chromatid exchange frequency. J. Histochem. Cytochem. 25 (7), 741–753.

Zeleke, T.B., Si, B.C., 2006. Characterizing scale-dependent spatial relationships between soil properties using multifractal techniques. Geoderma 134, 440–452.